



Cite this: *RSC Adv.*, 2020, 10, 19077

# Enhanced electrochemical performance of MoS<sub>2</sub>/graphene nanosheet nanocomposites†

Jin-Hyeok Choi, Min-Cheol Kim, Sang-Hyun Moon, Hyeona Kim, Yo-Seob Kim and Kyung-Won Park \*

Molybdenum disulfide (MoS<sub>2</sub>) is attractive as an anode material for next-generation batteries, because of its layered structure being favorable for the insertion/deinsertion of Li<sup>+</sup> ions, and its fairly high theoretical capacity. However, since the MoS<sub>2</sub> anode material has exhibited disadvantages, such as low electrical conductivity and poor cycling stability, to improve the electrochemical performance of MoS<sub>2</sub> in this study, a nanocomposite structure consisting of MoS<sub>2</sub> and GNS (MoS<sub>2</sub>/GNS) as an anode for LIBs was prepared, by controlling the weight ratios of MoS<sub>2</sub>/GNS. The X-ray diffraction patterns and electron microscopic analysis showed that the nanocomposite electrode structure consisted of well-formed MoS<sub>2</sub> nanoparticles and GNS. Compared to MoS<sub>2</sub>-only, the MoS<sub>2</sub>/GNS composites exhibited high retention and improved capacity at high current densities. In particular, among these nanocomposite samples, MoS<sub>2</sub>/GNS(8 : 2) with an appropriate portion of GNS exhibited the best LIB performance, due to the lowest interfacial resistance and highest Li-ion diffusivity.

Received 20th April 2020

Accepted 26th April 2020

DOI: 10.1039/d0ra03539d

rsc.li/rsc-advances

## 1 Introduction

Lithium-ion batteries (LIBs) are energy devices that convert chemical energy to electrical energy using electrochemical reactions, *i.e.*, reduction and oxidation between Li<sup>+</sup> ions and active electrode materials.<sup>1–3</sup> The electrochemical reduction and oxidation reactions spontaneously occur at the cathode and anode, respectively. In particular, the anode materials require typical characteristics, such as relatively low standard electrode potential, stable structure during the reactions with Li<sup>+</sup> ions, large diffusion coefficient, high electrical conductivity, and excellent reversibility of the reaction with Li<sup>+</sup> ions.<sup>4</sup> Typically, the anodes for LIBs exhibit one of three reaction mechanisms (insertion, conversion, and alloying), during electrochemical reaction between Li<sup>+</sup> ions and active anode material.<sup>5</sup> According to the insertion reaction, Li<sup>+</sup> ions are stored in the structure of the active material (M) with relatively low capacity, such as Li<sub>4</sub>Ti<sub>5</sub>O<sub>12</sub>, TiO<sub>2</sub>, and MoO<sub>3</sub>, as follows: Li<sup>+</sup> + M<sub>x</sub>X<sub>z</sub> → Li<sub>x</sub>M<sub>y</sub>X<sub>z</sub>. The alloying materials, such as Si, Ge, and Sn, with high theoretical capacities and serious volumetric variation during cycling exhibit the alloying reaction of Li<sup>+</sup> + M → Li<sub>x</sub>M. Finally, the active materials, such as CoO, NiO, and MoO<sub>3</sub>, with relatively high capacities, low efficiencies, and low cell voltages exhibit charging/discharging during the conversion reaction, such as Li<sup>+</sup> + M<sub>y</sub>X<sub>z</sub> → yM + Li<sub>x</sub>X<sub>z</sub>.<sup>6</sup>

Molybdenum disulfide (MoS<sub>2</sub>) has been attractive as an anode material for next-generation batteries, because of its layered structure being favorable for the insertion/deinsertion of Li<sup>+</sup> ion, and a fairly high theoretical capacity of 670 mA h g<sup>−1</sup>.<sup>7–12</sup> However, MoS<sub>2</sub> anode material has exhibited disadvantages, such as low electrical conductivity, and poor cycling stability, because of the low electric conductivity and the solid electrolyte interphase (SEI) layer during the conversion reaction.<sup>13–15</sup> Recently, to compensate the electrochemical properties of the MoS<sub>2</sub> anode for LIBs, carbon-based materials have been used for composite electrode structures, because of their excellent electrical conductivity, high specific surface area, and stability.<sup>16–18</sup> In particular, the composite electrodes consisting of MoS<sub>2</sub> and carbon can suppress the shuttling phenomenon of lithium polysulfides as by-products of the electrochemical reactions of MoS<sub>2</sub> with Li<sup>+</sup> ions, resulting in the improved cycling performance of the composite electrodes.<sup>19–21</sup> Mengmeng *et al.* reported a hybrid electrode consisting of vertically aligned MoS<sub>2</sub> and nitrogen-doped carbon with improved cycling properties for 300 cycles and a high capacity of 995 mA h g<sup>−1</sup> at 0.2 A g<sup>−1</sup>.<sup>22</sup> Wang *et al.* confirmed that the MoS<sub>2</sub> anode structure with three-dimensional fibrous nitrogen-doped carbon sphere exhibited a high capacity of 700 mA h g<sup>−1</sup> at 1.2 A g<sup>−1</sup> for 400 cycles.<sup>23</sup> The MoS<sub>2</sub>-based nanostructured electrode synthesized with nano-Si and carbon maintained a fairly high capacity of 767 mA h g<sup>−1</sup> at 100 mA g<sup>−1</sup> for 400 cycles.<sup>24</sup> In particular, graphene nanosheet (GNS) exhibits a 2-dimensional layered graphitic nanostructure with a weak van der Waals force between layers, and has offers, such as high electrical conductivity, and high specific surface area.<sup>25–27</sup> Thus,

Department of Chemical Engineering, Soongsil University, Seoul 06978, Republic of Korea. E-mail: kwpark@ssu.ac.kr; Fax: +82-2-812-5378; Tel: +82-2-820-0613

† Electronic supplementary information (ESI) available. See DOI: 10.1039/d0ra03539d



in this study, to improve the electrochemical performance of MoS<sub>2</sub>, a nanocomposite structure consisting of MoS<sub>2</sub> and GNS (MoS<sub>2</sub>/GNS) as an anode for LIBs was prepared by controlling the weight ratios of MoS<sub>2</sub>/GNS. The electrochemical properties of the MoS<sub>2</sub>/GNS nanocomposite samples were characterized and evaluated using coin-type cells.

## 2 Experimental

### 2.1. Synthesis of MoS<sub>2</sub> and GNS

To prepare the MoS<sub>2</sub>/GNS nanocomposites, the precursor for MoS<sub>2</sub> nanoparticle was firstly synthesized. Ammonium molybdate (0.88 g, (NH<sub>4</sub>)<sub>6</sub>Mo<sub>7</sub>O<sub>24</sub>·4H<sub>2</sub>O, Sigma-Aldrich) and sodium sulfide nonahydrate (2.64 g, Na<sub>2</sub>S·9H<sub>2</sub>O, Sigma-Aldrich) were mixed in 0.8 M HCl solution (100 mL) at 80 °C with stirring for 30 min. Hydroxylamine hydrochloride (0.7 g, NH<sub>2</sub>OH·HCl, Sigma-Aldrich) was added to the precursor solution at 80 °C, and then mixed with continuous stirring for 90 min. After the complete reaction, the dark brown precipitate was washed with de-ionized (DI) water and ethanol and dried in a 50 °C oven for 24 h. The GNS was obtained by mixing graphene (Graphene Supermarket) in a solution of H<sub>2</sub>SO<sub>4</sub> : HNO<sub>3</sub> = 3 : 1 at 120 °C for 2 h, washing with de-ionized (DI) water, and drying using a freeze-dryer.

### 2.2. Synthesis of MoS<sub>2</sub>/GNS

The MoS<sub>2</sub> precursor and GNS with different weight ratios of 9 : 1, 8 : 2, and 7 : 3 were added to 50 mL *N*-methyl-2-pyrrolidone (NMP) solution and then mixed with ultrasonication for 4 h (denoted respectively) (Fig. 1). The resulting precipitate was washed using ethanol and DI water and then dried in a 50 °C oven for 12 h. Finally, the dried sample was heated in an N<sub>2</sub> atmosphere at 500 °C for 3 h.

### 2.3. Materials characterization

The crystal structure of the as-prepared samples was characterized by an X-ray diffractometry (XRD, Bruker, D2 Phase system) operating at 40 kV and 100 mA with an X-ray source of Cu K<sub>α</sub> (λ = 0.15418 nm) and a Ni filter. The morphology of the samples was confirmed using field-emission scanning electron spectroscopy (FE-SEM, ZEISS, Gemini 300). The morphology and crystal structure of the samples were characterized by Cs-corrected transmission electron microscopy (Cs-TEM, JEM-ARM200F, JEOL Ltd, Japan). Thermogravimetric analysis (TGA) were conducted using a thermal analyzer (SDTA851, Mettler Toledo) in the range of 25 to 700 °C under an air flow of

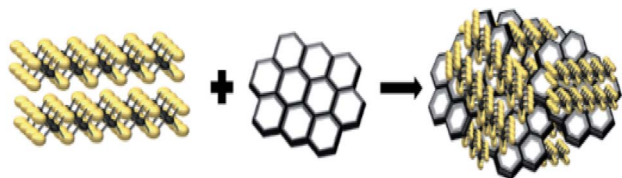


Fig. 1 Schematic illustration of the synthetic process of the MoS<sub>2</sub>/GNS nanocomposite.

50 cm<sup>3</sup> min<sup>-1</sup>. Raman spectroscopy analysis was performed using a DM2700 Raman spectroscope (RENISHAW, 2GTE70) with the excitation wavelength of 532 nm of Nd:YAG laser.

### 2.4. Cell assembly and electrochemical characterization

To characterize the electrochemical properties of the samples, coin-type half-cells with the samples as anodes were prepared in an Ar-filled glove box. The slurry was prepared using a paste mixer with the as-prepared powder samples as active materials (80 wt%), Ketjen black as a conducting agent (10 wt%), and polyvinylidene fluoride (PVDF, 10 wt%) as a binder. The as-prepared slurry was coated on a Cu foil using the doctor blade method, and then dried in a 110 °C convection oven for 24 h. The half-cell was assembled with an active material-coated electrode, 1.1 M LiPF<sub>6</sub> as an electrolyte, polyethylene as a separator, and lithium metal as a counter electrode. Charge-discharge curves of the samples were obtained by a multi-channel battery tester (WBCS3000L, Wonatech Co.) in the potential range of 0–3 V vs. Li/Li<sup>+</sup> with various current densities of 100, 200, 500, 1000, and 2000 mA g<sup>-1</sup>. Cyclic voltammograms (CVs) of the samples were measured at a scan rate of 0.2 mV s<sup>-1</sup> in the potential range of 0–3 V vs. Li/Li<sup>+</sup>. The interface resistances of the cells were measured by electrochemical impedance spectroscopy (EIS). To measure Li-ion conductivity for the samples, galvanostatic intermittent titration technique (GITT) measurement was performed at a current density of 100 mA g<sup>-1</sup> for 10 min intervals, with rest periods of 10 min, in the potential range of 0–2 V Li/Li<sup>+</sup>. The electrical conductivity of the samples was obtained by measuring *I*-*V* curves using a conductivity kit.

## 3 Results and discussion

Fig. 2 shows XRD patterns of MoS<sub>2</sub>/GNS 9 : 1, MoS<sub>2</sub>/GNS 8 : 2, MoS<sub>2</sub>/GNS 7 : 3, and MoS<sub>2</sub>-only prepared in the absence of GNS. All of the samples contained XRD peaks at 14.4°, 32.7°, 39.6°, 49.8°, and 58.3°, corresponding to the (002), (100), (103), (105), and (110) planes, with the MoS<sub>2</sub> crystal structure (PDF-65-1951) with lattice parameters of *a* = 3.16 Å, *c* = 12.30 Å, without diffraction peaks related to impurities or molybdenum oxides. In particular, MoS<sub>2</sub>/GNS 9 : 1, MoS<sub>2</sub>/GNS 8 : 2, and MoS<sub>2</sub>/GNS 7 : 3 exhibited a distinct peak at 26.5° associated with the (002) plane of graphene crystal structure as well as the characteristic peaks corresponding to the MoS<sub>2</sub> structure.<sup>28,29</sup> The average

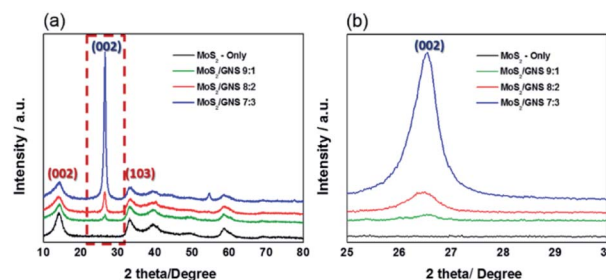


Fig. 2 Wide-range XRD patterns of the as-prepared MoS<sub>2</sub>/GNS samples as anodes.



particle sizes of MoS<sub>2</sub>/GNS 9 : 1, MoS<sub>2</sub>/GNS 8 : 2, MoS<sub>2</sub>/GNS 7 : 3, and MoS<sub>2</sub>-only were determined to be 3.97, 3.47, 4.47, and 4.48 nm, respectively, using the Scherrer equation. The order of the particle size in the samples is as follows: MoS<sub>2</sub>/GNS 7 : 3 ~ MoS<sub>2</sub>/GNS 8 : 2 < MoS<sub>2</sub>/GNS 9 : 1 ~ MoS<sub>2</sub>-only. According to the present synthesis, the MoS<sub>2</sub> precursor and GNS with different weight ratios were heated in an N<sub>2</sub> atmosphere at 500 °C for 3 h. Thus, as the content of GNS increased in the synthesis, the particle size of MoS<sub>2</sub> structure decreased. This demonstrates the GNS could hinder the growth of MoS<sub>2</sub> nanoparticles. In the Raman spectra of the samples, the E<sub>2g</sub>1 and A<sub>1g</sub> peaks at ~380 and ~408 cm<sup>-1</sup>, correspond to Mo–S and S vibrations in MoS<sub>2</sub> structure (Fig. S1(a)†). The D- and G-bands at ~1350 and ~1584 cm<sup>-1</sup>, correspond to the disorder and crystal structure of carbon, respectively, with a low I<sub>D</sub>/I<sub>G</sub>, demonstrating the high crystallinity of the carbon structure (Fig. S1(b)†).<sup>30–32</sup> Thus, it can be inferred that a nanocomposite electrode structure consisting of MoS<sub>2</sub> nanoparticles and GNS could be formed as an anode for LIBs.

The morphology and particle size of the samples were observed through SEM analysis (Fig. 3). Compared to MoS<sub>2</sub>-only, for the MoS<sub>2</sub>/GNS samples, MoS<sub>2</sub> nanoparticles were homogeneously mixed with 2-dimensional GNS structure. As the content of GNS increased in the synthesis, the portion of GNS increased as the particle size of MoS<sub>2</sub> decreased. The structure of the samples was characterized using TEM analysis (Fig. 4). The interplanar spacing of the samples was determined from the HR-TEM images to be ~0.620 nm corresponding to that of the (002) plane of MoS<sub>2</sub>. The average particle sizes of MoS<sub>2</sub>/GNS 9 : 1, MoS<sub>2</sub>/GNS 8 : 2, MoS<sub>2</sub>/GNS 7 : 3, and MoS<sub>2</sub>-only were determined to be 3.9, 3.6, 3.7, and 4.4 nm, respectively, which were in good agreement with those from the XRD analysis (Fig. S2†). To investigate the contents in the samples, TGA was performed with the samples in the temperature range of 25–950 °C under an air atmosphere (Fig. S3†). The weight losses at 25–200 °C and ~300 °C might result from an evaporation of water molecules in the samples and the transition of MoS<sub>2</sub> to

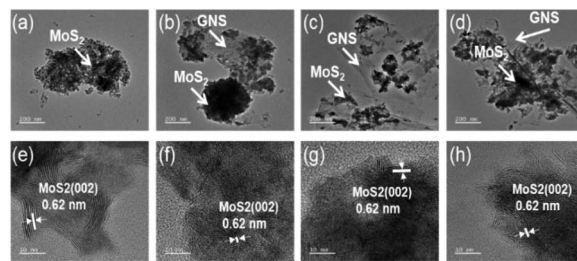


Fig. 4 TEM images of (a and e) MoS<sub>2</sub>-only, (b and f) MoS<sub>2</sub>/GNS 9 : 1, (c and g) MoS<sub>2</sub>/GNS 8 : 2 and (d and h) MoS<sub>2</sub>/GNS 7 : 3.

MoO<sub>3</sub>, respectively. Furthermore, the weight loss at >400 °C implies the content of carbon, resulting from the carbon oxidation. Thus, the contents of carbon in MoS<sub>2</sub>/GNS 9 : 1, MoS<sub>2</sub>/GNS 8 : 2, and MoS<sub>2</sub>/GNS 7 : 3 were 9.5, 32.7, and 45.6 wt%, respectively.<sup>33,34</sup> The electrical conductivity values of MoS<sub>2</sub>-only, MoS<sub>2</sub>/GNS 9 : 1, MoS<sub>2</sub>/GNS 8 : 2, and MoS<sub>2</sub>/GNS 7 : 3 were 2.1 × 10<sup>-3</sup>, 2.693, 3.545, and 1.420 S cm<sup>-1</sup>, respectively, demonstrating an excellent electronic motion of the composite structure.

Fig. 5 shows the charge/discharge characteristic curves of the samples as anodes measured at a current density of 200 mA g<sup>-1</sup> in the potential range of 0–3 V vs. Li/Li<sup>+</sup> for 100 cycles. After an initial activation cycling, the discharge capacities of MoS<sub>2</sub>/GNS 9 : 1, MoS<sub>2</sub>/GNS 8 : 2, MoS<sub>2</sub>/GNS 7 : 3, and MoS<sub>2</sub>-only measured after the 3<sup>rd</sup> cycle were 686, 662, 542, and 760 mA h g<sup>-1</sup>, respectively. The MoS<sub>2</sub>/GNS composite samples exhibited a lower initial capacity than that of the MoS<sub>2</sub>-only. Furthermore, the discharge capacities of MoS<sub>2</sub>/GNS 9 : 1, MoS<sub>2</sub>/GNS 8 : 2, MoS<sub>2</sub>/GNS 7 : 3, and MoS<sub>2</sub>-only after 100 cycles were 278, 613, 213, and 159 mA h g<sup>-1</sup>, respectively. The retentions of MoS<sub>2</sub>/GNS 9 : 1, MoS<sub>2</sub>/GNS 8 : 2, MoS<sub>2</sub>/GNS 7 : 3, and MoS<sub>2</sub>-only were 40.5%, 92.6%, 39.2%, and 20.9%, respectively. After 100 cycles, compared to the MoS<sub>2</sub>-only, composite anodes showed relatively relieved aggregation effect between the electrochemically active particles during cycling (Fig. S4†). As compared to the MoS<sub>2</sub>-based anode in the literatures, MoS<sub>2</sub>/GNS 8 : 2 exhibited fairly improved electrochemical performance, *i.e.* a discharge capacity of 613 mA h g<sup>-1</sup> at 200 mA g<sup>-1</sup> and a retention of 92.6%

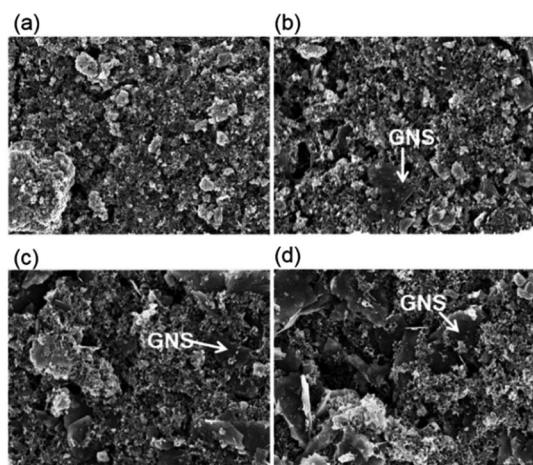


Fig. 3 SEM images of (a) MoS<sub>2</sub>-only, (b) MoS<sub>2</sub>/GNS 9 : 1, (c) MoS<sub>2</sub>/GNS 8 : 2, and (d) MoS<sub>2</sub>/GNS 7 : 3.

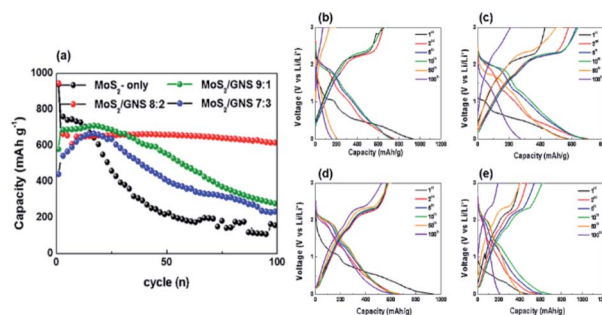


Fig. 5 (a) Cycle performances of MoS<sub>2</sub>/GNS electrodes at 200 mA g<sup>-1</sup>. Charge–discharge profiles of (b) MoS<sub>2</sub>-only, (c) MoS<sub>2</sub>/GNS 9 : 1, (d) MoS<sub>2</sub>/GNS 8 : 2, and (e) MoS<sub>2</sub>/GNS 7 : 3 measured at a current density of 200 mA g<sup>-1</sup>.



after 100 cycles (Table S1†).<sup>8,24,35–38</sup> The MoS<sub>2</sub>/GNS samples, despite relatively low capacities, exhibited significantly improved cycling performance, because of the enhanced stability of the nanocomposite structure with GNS during the conversion reaction. For the nanocomposite electrodes, the GNS with chemical and structural stability, excellent electrical properties, and high specific surface area can enhance the electrical conductivity, improving the cycling performance. To characterize the electrochemical properties of the samples, the CVs were measured at a scan rate of 0.2 mV s<sup>-1</sup> in the potential range of 0–3 V vs. Li/Li<sup>+</sup> (Fig. 6). In the 1st cycle during a cathodic potential scanning, lithium intercalation and conversion reactions appeared at ~0.9 and ~0.5 V, respectively (eqn (1) and (2)), forming the solid electrolyte interphase (SEI) layer on electrode surfaces from the decomposition products of electrolytes. The decomposition of Li<sub>x</sub>MoS<sub>2</sub> and oxidation of Li<sub>2</sub>S occurred at ~1.8 and ~2.4 V, respectively, during an anodic scanning (eqn (3) and (4)). Followed by the 1st scan, the electrochemical reduction reactions appeared at 1.3 V, respectively, during cathodic scanning in the subsequent cycles (eqn (4) and (5)).<sup>39–41</sup> In particular, the CVs for MoS<sub>2</sub>/GNS composite samples contained the oxidation characteristic peaks at 0.2 V associated with an intercalation of GNS as an anode, compared to MoS<sub>2</sub>-only without GNS.

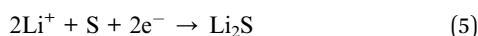
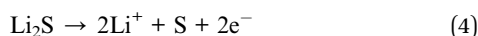
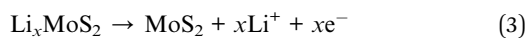
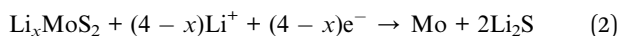
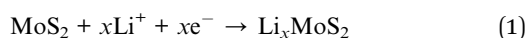


Fig. 7 shows the rate cycling performance of the samples as cathodes measured at various current densities from 100 to 2000 mA g<sup>-1</sup> in the potential range of 0–3 V for five cycles each. The average capacities of MoS<sub>2</sub>-only at 100, 200, 500, 1,000, 2,000, 100, and 200 mA g<sup>-1</sup> were 732, 442, 166, 64, 28, 264, and 119 mA h g<sup>-1</sup>, respectively. The average capacities of MoS<sub>2</sub>/GNS 9 : 1 at 100, 200, 500, 1,000, 2,000, 100, and 200 mA g<sup>-1</sup> were 817, 721, 545, 386, 261, 887, and 556 mA h g<sup>-1</sup>, respectively. The average capacities of MoS<sub>2</sub>/GNS 8 : 2 at 100, 200, 500, 1,000, 2,000, 100, and 200 mA g<sup>-1</sup> were 822, 764, 623, 480, 323, 879, and 736 mA h g<sup>-1</sup>, respectively. The average capacities of MoS<sub>2</sub>/

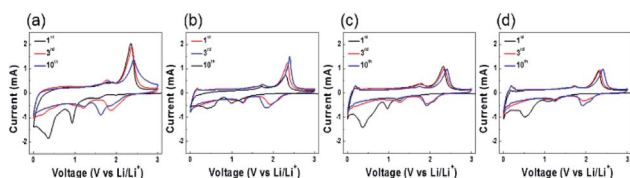


Fig. 6 CV curves of (a) MoS<sub>2</sub>-only, (b) MoS<sub>2</sub>/GNS 9 : 1, (c) MoS<sub>2</sub>/GNS 8 : 2, (d) MoS<sub>2</sub>/GNS 7 : 3 in the 1<sup>st</sup>, 3<sup>rd</sup>, 10<sup>th</sup> scans at a scan rate of 0.2 mV s<sup>-1</sup> in the potential range of 0.0–3.0 V vs. Li/Li<sup>+</sup>.

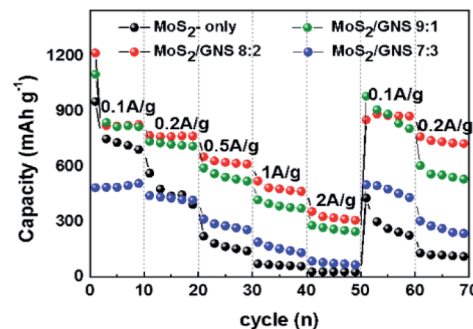


Fig. 7 High-rate performance of the MoS<sub>2</sub>/GNS anodes measured at varying current densities for each 10 cycles.

GNS 7 : 3 at 100, 200, 500, 1,000, 2,000, 100, and 200 mA g<sup>-1</sup> were 489, 430, 279, 154, 74, 479, and 264 mA h g<sup>-1</sup>, respectively. The MoS<sub>2</sub>/GNS composite samples exhibited improved high-rate performance and recovery rate because of the enhancement of electronic motion caused by GNS as an excellent conductor, compared to MoS<sub>2</sub>-only without GNS.

Fig. 8 compares the interfacial resistance ( $R_{ct}$ ) of the MoS<sub>2</sub>/GNS composites and MoS<sub>2</sub>-only after the 3<sup>rd</sup> cycle between electrolyte and electrode. The values of  $R_{ct}$  for MoS<sub>2</sub>-only, MoS<sub>2</sub>/GNS 9 : 1, MoS<sub>2</sub>/GNS 8 : 2, and MoS<sub>2</sub>/GNS 7 : 3 were 131, 20, 17, and 43 Ω, respectively. Compared to MoS<sub>2</sub>-only, the MoS<sub>2</sub>/GNS composites showed decreased resistance, resulting from the improved conductivity of the composite caused by GNS with excellent electrical conductivity. In particular, among these composites, MoS<sub>2</sub>/GNS 8 : 2 with an appropriate portion of GNS has the lowest interfacial resistance.<sup>42,43</sup> Furthermore, in the initial states, MoS<sub>2</sub>-only showed increased interfacial resistance whereas the MoS<sub>2</sub>/GNS composites maintained the low resistance due to the improved electrical and electrochemical properties by GNS (Fig. S5†). To determine the Li-ion conductivity of the samples as anodes, the GITT analysis was performed after the 3<sup>rd</sup> cycle.<sup>44</sup> Based on the diffusivity of Li<sup>+</sup> ion according to the state of charge (SOC), compared to MoS<sub>2</sub>-only, the MoS<sub>2</sub>/GNS composites exhibited overall improved ionic motion (Fig. 9a). Also, when compared to the average diffusivity, the MoS<sub>2</sub>/GNS composites exhibited higher values than MoS<sub>2</sub>-

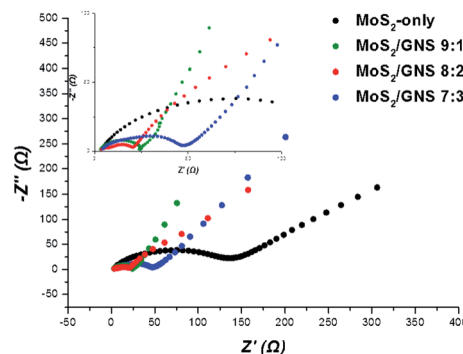


Fig. 8 Nyquist plots of the samples after 3 cycles at a current of 200 mA g<sup>-1</sup>.



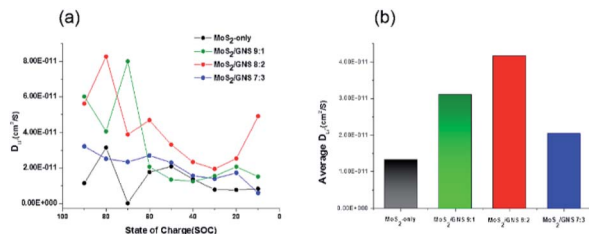


Fig. 9 The GITT analysis after the 3<sup>rd</sup> cycle. (a) Diffusivity of Li<sup>+</sup> ion according to the state of charge (SOC) and (b) the average Li<sup>+</sup> ion diffusion coefficients of the samples.

only (Fig. 9b). In particular, MoS<sub>2</sub>/GNS 8 : 2 showed the best Li-ion diffusivity. Thus, the improved LIB performance of MoS<sub>2</sub>/GNS 8 : 2 with a proper portion of GNS results from the lowest interfacial resistance and highest Li-ion diffusivity.

## 4 Conclusions

In summary, nanocomposite electrodes with MoS<sub>2</sub> and GNS were prepared to improve the electrochemical performance of MoS<sub>2</sub> as an anode for LIBs. The nanocomposite electrode structure was found to consist of MoS<sub>2</sub> nanoparticles and GNS. Compared to MoS<sub>2</sub>-only, the MoS<sub>2</sub>/GNS composites exhibited improved electrochemical performance, *i.e.* high retentions and improved capacities at high current densities. In particular, MoS<sub>2</sub>/GNS 8 : 2 with a proper portion of GNS exhibited improved LIB performance due to the lowest interfacial resistance between electrode and electrolyte and highest Li-ion diffusivity. Thus, the nanocomposite electrode consisting of MoS<sub>2</sub> and GNS can be utilized as an anode for high-performance LIBs.

## Conflicts of interest

There are no conflicts to declare.

## Acknowledgements

This work was supported by the National Research Foundation of Korea (NRF) grant funded by the Korea government (MSIT) (No.2020R1A2C2010510).

## Notes and references

- C. J. Northcott and M. B. Stein, *J. Clin. Psychiatry*, 1994, **55**, 539–542.
- P. Roy and S. K. Srivastava, *J. Mater. Chem. A*, 2015, **3**, 2454–2484.
- J. B. Goodenough and K. S. Park, *J. Am. Chem. Soc.*, 2013, **135**, 1167–1176.
- N. Nitta, F. Wu, J. T. Lee and G. Yushin, *Mater. Today*, 2015, **18**, 252–264.
- L. Ji, Z. Lin, M. Alcoutlabi and X. Zhang, *Energy Environ. Sci.*, 2011, **4**, 2682–2689.
- J. Lu, Z. Chen, F. Pan, Y. Cui and K. Amine, *Electrochem. Energy Rev.*, 2018, **1**, 35–53.
- N. Choudhary, M. Patel, Y. H. Ho, N. B. Dahotre, W. Lee, J. Y. Hwang and W. Choi, *J. Mater. Chem. A*, 2015, **3**, 24049–24054.
- G. Li, X. Zeng, T. Zhang, W. Ma, W. Li and M. Wang, *CrystEngComm*, 2014, **16**, 10754–10759.
- Z. He and W. Que, *Appl. Mater. Today*, 2016, **3**, 23–56.
- H. Wu, C. Hou, G. Shen, T. Liu, Y. Shao, R. Xiao and H. Wang, *Nano Res.*, 2018, **11**, 5866–5878.
- L. Chen, F. Chen, N. Tronganh, M. Lu, Y. Jiang, Y. Gao, Z. Jiao, L. Cheng and B. Zhao, *J. Mater. Res.*, 2016, **31**, 3151–3160.
- H. Yu, C. Zhu, K. Zhang, Y. Chen, C. Li, P. Gao, P. Yang and Q. Ouyang, *J. Mater. Chem. A*, 2014, **2**, 4551–4557.
- J. Zhao, H. Ren, C. Gu, W. Guan, X. Song and J. Huang, *J. Alloys Compd.*, 2019, **781**, 174–185.
- S. Hu, W. Chen, J. Zhou, F. Yin, E. Uchaker, Q. Zhang and G. Cao, *J. Mater. Chem. A*, 2014, **2**, 7862–7872.
- Y. Wang, M. Zhen, H. Liu and C. Wang, *J. Solid State Electrochem.*, 2018, **22**, 3069.
- M. Choi, S. K. Koppala, D. Yoon, J. Hwang, S. M. Kim and J. Kim, *J. Power Sources*, 2016, **309**, 202–211.
- G. H. Lee, S. J. Kim, M. C. Kim, H. S. Choe, D. M. Kim, S. B. Han, D. H. Kwak, J. H. Jeong and K. W. Park, *RSC Adv.*, 2016, **6**, 92259–92266.
- J. Shao, T. Gao, Q. Qu, Q. Shi, Z. Zuo and H. Zheng, *J. Power Sources*, 2016, **324**, 1–7.
- X. Fan, W. Sun, F. Meng, A. Xing and J. Liu, *Green Energy Environ.*, 2018, **3**, 2–19.
- Z. A. Ghazi, X. He, A. M. Khattak, N. A. Khan, B. Liang, A. Iqbal, J. Wang, H. Sin, L. Li and Z. Tang, *Adv. Mater.*, 2017, 1606817.
- X. Ji, S. Evers, R. Black and L. F. Nazar, *Nat. Commun.*, 2011, **2**, 325–327.
- M. Zhen, J. Wang, S. qi Guo and B. Shen, *Appl. Surf. Sci.*, 2019, **487**, 285–294.
- X. Wang, S. Fei, S. Huang, C. Wu, J. Zhao, Z. Chen, K. Uvdal and Z. Hu, *Carbon*, 2019, **150**, 363–370.
- P. Zhang, Q. Ru, H. Yan, X. Hou, F. Chen, S. Hu and L. Zhao, *J. Mater. Sci. Technol.*, 2019, **35**, 1840–1850.
- E. Yoo, J. Kim, E. Hosono, H. Zhou and T. Kudo, *Nano*, 2008, 13–18.
- J. Xu, Y. Lin, J. W. Connell and L. Dai, *Small*, 2015, **11**, 6179–6185.
- D. Graphene, S. As, A. Materials, S. Rate, L. Capacity and L. I. Batteries, *ACS Nano*, 2011, 5463–5471.
- Y. Liu, Y. Zhao, L. Jiao and J. Chen, *J. Mater. Chem. A*, 2014, **2**, 13109–13115.
- J. Wang, J. Tian, Naren, X. Wang, Z. Qin and Z. Shan, *Energy Technol.*, 2018, **6**, 1913–1920.
- H. Huang, Y. Xia, X. Tao, J. Du, J. Fang, Y. Gan and W. Zhang, *J. Mater. Chem.*, 2012, **22**, 10452–10456.
- W. Wu, J. Liu, X. Li, T. Hua, X. Cong, Z. Chen, F. Ying, W. Shen, B. Lu, K. Dou and X. Zhou, *Corros. Eng., Sci. Technol.*, 2018, **53**, 625–632.



- 32 H. Li, Q. Zhang, C. C. R. Yap, B. K. Tay, T. H. T. Edwin, A. Olivier and D. Baillargeat, *Adv. Funct. Mater.*, 2012, **22**, 1385–1390.
- 33 A. Bahuguna, S. Kumar, V. Sharma, K. L. Reddy, K. Bhattacharyya, P. C. Ravikumar and V. Krishnan, *ACS Sustainable Chem. Eng.*, 2017, **5**, 8551–8567.
- 34 X. Yang, H. Niu, H. Jiang, Q. Wang and F. Qu, *J. Mater. Chem. A*, 2016, **4**, 11264–11275.
- 35 H. Sun, J. G. Wang, W. Hua, J. Wang, D. Nan and B. Guo, *J. Alloys Compd.*, 2020, **821**, 153339.
- 36 X. Liu, X. Zhang, S. Ma, S. Tong, X. Han and H. Wang, *Electrochim. Acta*, 2020, **333**, 135568.
- 37 S. G. Stolyarova, V. O. Koroteev, K. I. Baskakova, A. A. Makarova, A. V. Okotrub and L. G. Bulusheva, *Fullerenes, Nanotubes, Carbon Nanostruct.*, 2020, **28**, 328–334.
- 38 F. Wang, F. Li, L. Ma and M. Zheng, *Chem.–Eur. J.*, 2019, **25**, 14598–14603.
- 39 Y. Hu, X. Li, A. Lushington, M. Cai, D. Geng, M. N. Banis, R. Li and X. Sun, *ECS J. Solid State Sci. Technol.*, 2013, **2**, 3034–3039.
- 40 T. Stephenson, Z. Li, B. Olsen and D. Mitlin, *Energy Environ. Sci.*, 2014, **7**, 209–231.
- 41 C. Feng, J. Ma, H. Li, R. Zeng, Z. Guo and H. Liu, *Mater. Res. Bull.*, 2009, **44**, 1811–1815.
- 42 J. Zhou, J. Qin, X. Zhang, C. Shi, E. Liu, J. Li, N. Zhao and C. He, *ACS Nano*, 2015, **9**, 3837–3848.
- 43 C. Zhao, X. Wang, J. Kong, J. M. Ang, P. S. Lee, Z. Liu and X. Lu, *ACS Appl. Mater. Interfaces*, 2016, **8**, 2372–2379.
- 44 Y. Kim, M. Kim, S. Moon, H. Kim and K. Park, *Electrochim. Acta*, 2020, **341**, 136045.

